MOX-Report No. 53/2022

Numerical simulation of the Athens 1999 earthquake including simplified models of the Acropolis and the Parthenon: initial results and outlook

Antonietti, P.F; Cauzzi, C.; Mazzieri, I.; Melas L.; Stupazzini, M.

MOX, Dipartimento di Matematica
Politecnico di Milano, Via Bonardi 9 - 20133 Milano (Italy)

mox-dmat@polimi.it http://mox.polimi.it

Numerical simulation of the Athens 1999 earthquake including simplified models of the Acropolis and the Parthenon: initial results and outlook

Paola F. Antonietti, Carlo Cauzzi, Ilario Mazzieri, Laura Melas and Marco Stupazzini

Abstract In this work we present a preliminary study of the seismic response of the Acropolis and of the Parthenon of Athens to the 1999 M_w 5.9 earthquake. The three-dimensional numerical model includes the surface topography of the Attica region, the seismogenic fault and the most important geological units in the metropolitan area of Athens, the Acropolis hill and the Parthenon. The multiscale numerical model, designed in order to correctly propagate seismic waves up to $5Hz$, is solved through a discontinuous Galerkin spectral element method implemented in the open source library SPEED `https://speed.mox.polimi.it`. Numerical results show the effectiveness of this approach and highlights new challenges for dynamic soil-structure interaction problems at regional scale.

1 Introduction

Understanding the physics of earthquakes and predicting their impact on the human and natural environment is of crucial importance for delineating and improving seismic risk reduction strategies. Nowadays, the most employed approaches to predict

Paola F. Antonietti, Ilario Mazzieri
MOX-Department of Mathematics, Politecnico di Milano, P.za L. da Vinci 32, Milano, Italy, e-mail: paola.antonietti@polimi.it, ilario.mazzieri@polimi.it

Carlo Cauzzi
Swiss Seismological Service (SED), ETH Zürich, Sonneggstrasse 5, 8092 Zürich, Switzerland e-mail: carlo.cauzzi@sed.ethz.ch

Laura Melas
Department of Mathematics, Technical University of Munich, Boltzmannstr. 3, 85748, Garching, Germany e-mail: melas@ma.tum.de

Marco Stupazzini
Munich RE, Geo Risks, Königinstr. *107*, *80802* Munich, Germany e-mail: MStupazzini@munichre.com

ground motion are: (i) empirical models, (e.g., ground motion prediction equations) and (ii) physics-based approaches (e.g., numerical solution to partial differential equations encoding the physics of the problem, from the rupture generation to soil structure interaction effects, cf. [1]). Nowadays, thanks to the ongoing progress of computational infrastructures, different discretization strategies have been developed and effectively applied to earthquake dynamics and seismic wave propagation problems, [2]. In this context, we recall the finite difference (FD) method, cf. e.g. [3, 4, 5], the Spectral Element Method (SEM), see e.g. [6, 7], the Arbitrary order DERivative Discontinuous Galerkin (ADER-DG) method, cf. e.g. [8, 9, 10, 11], and the Discontinuous Galerkin Spectral Element (DGSE) method, cf. e.g. [12, 13, 14]. In the recent years three-dimensional (3D) physics-based simulations, based on the DGSE method, have been employed for the study of real earthquake ground motion [15, 16, 17] and, more recently, for seismic risk scenarios in large urban areas [18, 19, 20]. However, accounting for the multi-scale nature of wave propagation within a single model poses challenging demands on computational methods and resources due to the coexistence of very different spatial scales, from few tens of kilometers, with reference to the seismic fault, up to few meters, or even less when considering the structural elements.

The aim of this study is to develop a numerical model that allows to correctly simulate an earthquake event in a source-site-structure mode. In particular, to consider in the same computational model the description of seismogenic sources, complex geological structures and soil-structure interactions.

In this way, numerical simulations provide as output the full waveform of ground motion compatible with the source rupture process, the source-to-site path and the local geological conditions, but also with the seismic response of the built environment.

The numerical results presented in this work are obtained using the high-performance open-source library SPEED, cf. also [21], which is based on high-order DGSE methods on hexahedral/tetrahedral meshes. SPEED can accurately simulate large-scale seismic events by including kinematic source models, arbitrarily complex geological structures and the built environment.

We demonstrate the approach by presenting a numerical simulation of the 1999 M_w 5.9 Athens (Greece) earthquake. The three-dimensional numerical model includes the surface topography of the Attica region, the seismogenic (Fili) fault, and the major geological features of the region, such as the Athens Schist, the Acropolis hill and the Parthenon.

The work is organized as follows. In Section 2 we recall the differential model and its numerical approximation by the DGSE method. In Section 3 we describe different geophysical and geological models used for the numerical simulations of the 1999 Athens earthquake. We discuss our numerical results in Section 4 and finally, in Section 5, we give a summary of the results achieved highlighting advantages and limitations of the proposed approach. Moreover we discuss possible future developments.

2 Mathematical model and its numerical discretization

Here and in the sequel, vectors are typed with bold letters, while underlined quantities denote matrices or tensors.

Let $\Omega \subset \mathbb{R}^3$ be an open bounded polyhedral domain (representing the portion of the ground where we investigate the wave propagation phenomena) and let $\partial\Omega$ be its boundary. We suppose $\partial\Omega$ to be decomposed into two disjoint portions Γ_N and Γ_{NR}, where Γ_N is a traction-free boundary while Γ_{NR} denotes the portion of $\partial\Omega$ where non-reflecting boundary conditions are prescribed, cf. [22]. Given a final observation time $T > 0$, we consider the dynamic equation of a viscoelastic material described by the following system:

$$\begin{cases} \rho \boldsymbol{u}_{tt} + 2\rho\xi \boldsymbol{u}_t - \nabla \cdot \underline{\sigma}(\mathbf{u}) + \rho\xi^2 \boldsymbol{u} = \boldsymbol{f}, & \text{in } \Omega \times (0,T], \\ \underline{\sigma}(\boldsymbol{u})\boldsymbol{n} = \mathbf{0}, & \text{on } \Gamma_N \times (0,T], \\ \underline{\sigma}(\boldsymbol{u})\boldsymbol{n} = \boldsymbol{t}^*, & \text{on } \Gamma_{NR} \times (0,T], \\ (\boldsymbol{u}, \boldsymbol{u}_t) = (\mathbf{0}, \mathbf{0}), & \text{in } \Omega \times \{0\}, \end{cases} \tag{1}$$

where $\boldsymbol{u} = \boldsymbol{u}(\boldsymbol{x}, t)$ is the displacement field, $\underline{\sigma}(\boldsymbol{u}) = \underline{\sigma}(\boldsymbol{x}, t)$ is the stress tensor, $\rho = \rho(\boldsymbol{x})$ is a piecewise constant strictly positive function describing the material density, $\boldsymbol{n} = \boldsymbol{n}(\boldsymbol{x})$ is the unit outward normal vector to $\partial\Omega$, $\xi = \xi(\mathbf{x}) > 0$ is a suitable decay factor with dimension inverse of time that models the damping effects, and $\boldsymbol{f} = \boldsymbol{f}(\boldsymbol{x}, t)$ is a given external load (e.g. the seismic source). On Γ_{NR} we impose a fictitious traction $\boldsymbol{t}^* = \boldsymbol{t}^*(\boldsymbol{u}, \boldsymbol{u}_t)$, defined as

$$\begin{bmatrix} t^*_{\tau_1} \\ t^*_{\tau_2} \\ t^*_{\boldsymbol{n}} \end{bmatrix} = \begin{bmatrix} \frac{\mu(2v_P - v_S)}{v_S} \frac{\partial}{\partial \tau_1}(\boldsymbol{u} \cdot \boldsymbol{n}) - \frac{\mu}{v_S} \frac{\partial}{\partial t}(\boldsymbol{u} \cdot \boldsymbol{\tau}_1) \\ \frac{\mu(2v_P - v_S)}{v_S} \frac{\partial}{\partial \tau_2}(\boldsymbol{u} \cdot \boldsymbol{n}) - \frac{\mu}{v_S} \frac{\partial}{\partial t}(\boldsymbol{u} \cdot \boldsymbol{\tau}_2) \\ \frac{\lambda v_S + 2\mu(v_P - v_S)}{v_S} \left[\frac{\partial}{\partial \tau_2}(\boldsymbol{u} \cdot \boldsymbol{\tau}_1) + \frac{\partial}{\partial \tau_1}(\boldsymbol{u} \cdot \boldsymbol{\tau}_2) \right] - \frac{\lambda + 2\mu}{v_S} \frac{\partial}{\partial t}(\boldsymbol{u} \cdot \boldsymbol{n}), \end{bmatrix}$$

being λ and μ the Lamé parameters, $v_P = \sqrt{(\lambda + 2\mu)/\rho}$ and $v_S = \sqrt{\mu/\rho}$ the characteristic compressional and shear wave velocities, respectively, $\boldsymbol{n}$ the outward pointing unit vector from Γ_{NR} and $\boldsymbol{\tau}_1$ and $\boldsymbol{\tau}_2$ two arbitrary mutually orthogonal unit vectors such that $\{\boldsymbol{\tau}_1, \boldsymbol{\tau}_2, \boldsymbol{n}\}$ defines a right handed Cartesian frame, see also [13]. We assume a linear constitutive equation for the stress tensor (Hooke's law) $\underline{\sigma}(\mathbf{u}) = \underline{D}\,\underline{\epsilon}(\boldsymbol{u})$ or alternatively

$$\begin{pmatrix} \sigma_{11} \\ \sigma_{22} \\ \sigma_{33} \\ \sigma_{23} \\ \sigma_{13} \\ \sigma_{12} \end{pmatrix} = \begin{pmatrix} \lambda + 2\mu & \lambda & \lambda & 0 & 0 & 0 \\ \lambda & \lambda + 2\mu & \lambda & 0 & 0 & 0 \\ \lambda & \lambda & \lambda + 2\mu & 0 & 0 & 0 \\ 0 & 0 & 0 & \mu & 0 & 0 \\ 0 & 0 & 0 & 0 & \mu & 0 \\ 0 & 0 & 0 & 0 & 0 & \mu \end{pmatrix} \begin{pmatrix} \epsilon_{11} \\ \epsilon_{22} \\ \epsilon_{33} \\ 2\epsilon_{23} \\ 2\epsilon_{13} \\ 2\epsilon_{12} \end{pmatrix},$$

where $\underline{\epsilon}(\boldsymbol{u}) = (\nabla \boldsymbol{u} + \nabla \boldsymbol{u}^T)/2$ is the strain tensor, and $\underline{D}$ is the fourth order symmetric and positive definite elasticity tensor. Here, we suppose $\underline{D}$ to be piecewise constant, i.e. the Lamé parameters λ and μ are piecewise constant in Ω.

The seismic source $\boldsymbol{f}$ in (1) represents a kinematic finite-fault model expressed in terms of a distribution of double-couple point sources. In particular, we express the latter through the relation $\boldsymbol{f}(\boldsymbol{x},t) = -\nabla \cdot m(\boldsymbol{x},t)$, cf. [23], being $m(\boldsymbol{x},t)$ the seismic moment tensor defined as

$$m_{ij}(\boldsymbol{x},t) = \frac{M_0(\boldsymbol{x},t)}{V}(s_i\nu_j + s_j\nu_i), \quad i,j = 1,\dots,3.$$

In the above equation $\boldsymbol{\nu} = (\nu_1,\nu_2,\nu_3)$ and $\boldsymbol{s} = (s_1,s_2,s_2)$ are the fault normal and the unit slip vectors along the fault, respectively, and $M_0(\boldsymbol{x},t)$ is the time history of the moment release at the source point $\boldsymbol{x}$ inside the elementary volume V.

Next, we briefly recall the DGSE formulation of problem (1). We refer the reader to [12, 24] for a detailed analysis of the method and to [21] for its implementation in SPEED. First, we subdivide Ω into K non-overlapping regions Ω_k, $k = 1,\dots,K$, such that $\Omega = \cup_{k=1}^{K}\Omega_k$, and we define the skeleton $\mathcal{S}$ to be the collection of the interfaces between subdomains. Note that this (macro) decomposition can be geometrically non-conforming. Then, within each subdomain Ω_k, we consider a grid $\mathcal{T}_{h_k}$ made of hexahedral elements and assign a polynomial approximation degree $N_k \geq 1$. Notice that mesh generation is performed independently on each subdomain Ω_k and also the local polynomial degree N_k can vary subdomainwise. We define $\mathcal{T}_h$ to be the union of the (independently generated) grids $\mathcal{T}_{h_k}$, and collect all the element faces (here a face is the non empty interior of the intersection of two neighboring hexahedral elements that belong to $\mathcal{T}_h$) that lie on $\mathcal{S}$ in the set $\mathcal{F}_h^I$. Moreover, we also collect boundary faces in the set $\mathcal{F}_h^B = \mathcal{F}_h^N \cup \mathcal{F}_h^{NR}$, being $\mathcal{F}_h^* = \mathcal{F}_h^B \cap \Gamma_*$, $* = \{N, NR\}$. implicit in this definition there is the assumption that the mesh respect the decomposition of the boundary $\partial\Omega$ into the set Γ_R and Γ_{NR}. We denote by $\mathbf{V}_{DG}$ the discrete space of functions that are elementwise continuous polynomials of degree N_k in each coordinate direction in each subdomain Ω_k, and that can be discontinuous across $\mathcal{S}$, i.e. $\mathbf{V}_{DG} = \{\boldsymbol{v} \in \mathbf{L}^2(\Omega) : \mathbf{v} \in C^0(\Omega_k),\ k = 1,...K,\ \text{and } v|_E \in \mathbb{P}^{p_k}(E)\ \forall E \in \mathcal{T}_{h_k}\}$. Then, the semi-discrete DGSE formulation reads as follows: for any $t \in (0,T]$, find $\boldsymbol{u}^h = \boldsymbol{u}^h(t) \in \mathbf{V}_{DG}$ such that

$$\begin{aligned}\int_{\mathcal{T}_h} \rho \boldsymbol{u}^h_{tt} \cdot \boldsymbol{v}\, d\boldsymbol{x} + \int_{\mathcal{T}_h} 2\rho\xi \boldsymbol{u}^h_t \cdot \boldsymbol{v}\, d\boldsymbol{x} + \int_{\mathcal{T}_h} \rho\xi^2 \boldsymbol{u}^h \cdot \boldsymbol{v}\, d\boldsymbol{x} + \mathcal{A}_h(\boldsymbol{u}^h,\boldsymbol{v}) \\ = \int_{\mathcal{T}_h} \boldsymbol{f}(t) \cdot \boldsymbol{v}\, d\boldsymbol{x} + \int_{\mathcal{F}_h^{NR}} \boldsymbol{t}^*(t) \cdot \boldsymbol{v}\, d\boldsymbol{s},\end{aligned} \tag{2}$$

for any $\boldsymbol{v} \in \mathbf{V}_{DG}$, where

$$\begin{aligned}\mathcal{A}_h(\boldsymbol{u},\boldsymbol{v}) = \int_{\mathcal{T}_h} \underline{\sigma}(\boldsymbol{u}) : \underline{\epsilon}(\boldsymbol{v})\, d\boldsymbol{x} - \int_{\mathcal{F}_h^I} \{\underline{\sigma}(\boldsymbol{u})\} : [[\boldsymbol{v}]]\, d\boldsymbol{s} \\ - \int_{\mathcal{F}_h^I} [[\boldsymbol{u}]] : \{\underline{\sigma}(\boldsymbol{v})\}\, d\boldsymbol{s} + \int_{\mathcal{F}_h^I} \eta [[\boldsymbol{u}]] : [[\boldsymbol{v}]]\, d\boldsymbol{s}.\end{aligned}$$

On each face $F \in \mathcal{F}_h^I$ shared by two neighbouring elements $E_i \subset \Omega_i$ and $E_j \subset \Omega_j$ we define the average $\{\cdot\}$ and jump $[[\cdot]]$ operators (see [25, 24]) in the following way:

$$\{\mathbf{v}\} = \frac{1}{2}(\boldsymbol{v}_i + \boldsymbol{v}_j), \qquad [[\boldsymbol{v}]] = \boldsymbol{v}_i \otimes \boldsymbol{n}_i + \boldsymbol{v}_j \otimes \boldsymbol{n}_j,$$
$$\{\underline{\tau}\} = \frac{1}{2}(\underline{\tau}_i + \underline{\tau}_j), \qquad [[\underline{\tau}]] = \underline{\tau}_i \boldsymbol{n}_i + \underline{\tau}_j \boldsymbol{n}_j,$$

where $\boldsymbol{a} \otimes \boldsymbol{b} \in \mathbb{R}^{3\times 3}$ is the tensor with entries $(\boldsymbol{a} \otimes \boldsymbol{b})_{mn} = a_m b_n$, $m, n = 1, 2, 3$, for all $\boldsymbol{a}, \boldsymbol{b} \in \mathbb{R}^3$ and $\boldsymbol{n}_i$ (resp. $\boldsymbol{n}_j$) is the unit normal vector to F pointing outward to Ω_i (resp. Ω_j).

The penalty parameter η is defined as $\eta = \alpha\{\lambda + 2\mu\}_A \frac{\mathtt{N}^2}{\mathtt{h}}$, being $\{q\}_A = 2q^+q^-/(q^+ + q^-)$ the harmonic average of the quantity q across F, α a (large enough) positive constant to be properly chosen, cf. e.g. [25], and $\mathtt{N}$ and $\mathtt{h}$ defined on each face $F \in \mathcal{F}_h^I$ as $\mathtt{N} = \max\{N_i, N_j\}$ and $\mathtt{h} = \min\{h_i, h_j\}$.

Well-posedness and stability results and a-priori error bounds for the DGSE formulation (2) can be found in [26, 27, 12, 28, 29].

Next, by introducing a suitable basis $\{\boldsymbol{\Phi}_i\}_{i=1}^{N_{dof}}$ for the finite element space $\boldsymbol{V}_{DG}$, it is possible to obtain the following second-order system of ordinary differential equations supplemented with suitable initial conditions:

$$\underline{\boldsymbol{M}}\ddot{\boldsymbol{U}}(t) + \underline{\boldsymbol{C}}\dot{\boldsymbol{U}}(t) + \underline{\boldsymbol{K}}\boldsymbol{U}(t) = \boldsymbol{F}(t), \quad t \in (0, T]. \tag{3}$$

Here, $\boldsymbol{U}$ is the vector containing the expansion coefficients U_i with respect to the chosen basis and $\dot{\boldsymbol{U}}$ and $\ddot{\boldsymbol{U}}$ are the vectors of nodal velocity and acceleration, respectively. The mass, damping and stiffness matrices in (3) are defined as

$$\underline{M}_{ij} = \int_{\mathcal{T}_h} \rho \boldsymbol{\Phi}_j \cdot \boldsymbol{\Phi}_i \, d\boldsymbol{x}, \qquad i, j = 1, ..., N_{dof},$$
$$\underline{C}_{ij} = \int_{\mathcal{T}_h} 2\rho\xi \boldsymbol{\Phi}_j \cdot \boldsymbol{\Phi}_i \, d\boldsymbol{x}, \qquad i, j = 1, ..., N_{dof}$$
$$\underline{K}_{ij} = \mathcal{A}_h(\boldsymbol{\Phi}_j, \boldsymbol{\Phi}_i) + \int_{\mathcal{T}_h} \rho\xi^2 \boldsymbol{\Phi}_j \cdot \boldsymbol{\Phi}_i \, d\boldsymbol{x}, \quad i, j = 1, ..., N_{dof},$$

and $\boldsymbol{F}$ is the vector of the external applied loads defined as

$$\boldsymbol{F}_i(t) = \int_{\mathcal{T}_h} \boldsymbol{f}(t) \cdot \boldsymbol{\Phi}_i \, d\boldsymbol{x} + \int_{\mathcal{F}_h^{NR}} \boldsymbol{t}^*(t) \cdot \boldsymbol{\Phi}_i, \, d\boldsymbol{s} \qquad i = 1, ..., N_{dof}.$$

To integrate in time (3) we consider the second-order accurate and explicit leap-frog scheme as proposed in [24].

3 Computational setting for the September 7, 1999 Athens earthquake

On September 7, 1999 at 14:56:50 (local time) an earthquake of magnitude M_w 5.9 struck Attica region (Greece) within a few kilometers from the center of the city of Athens, cf. [30]. Major damages were observed, especially in the north–northwest part of the city, close to the earthquake rupture. 143 people were killed, more than 2000 were injured and over a hundred buildings collapsed. On the other hand, historical monuments were nearly untouched except for small permanent displacements observed at some columns [31, 32, 33, 34, 35, 36]. The Acropolis of Athens, a worldwide renowned symbol of the cultural and historical heritage of Greece within the context of western civilization, hosts the Parthenon, one the most important surviving buildings of Classical Greece, generally considered the apotheosis of the Doric order. Within the last two decades extensive restoration and conservation works have been carried out in the Acropolis of Athens, focusing on the Parthenon, that also include a seismic monitoring network [37, 38].

We present physics-based simulations of the ground shaking generated in Athens (Greece) by the September 7 1999 earthquake occurred on in the proximity of the metropolitan area (see `https://esm-db.eu/#/event/GR-1999-0001`) based on employing the model introduced in Section 2. The computational domain comprises the earthquake source, the crustal layering, the major geological features of the Athenian basin, the Acropolis and a simplified model of the Parthenon. The complexity of the problem at hand requires adopting a multi-scale approach. In particular, all the components of the numerical model were designed to account for: (i) the large variations of the characteristic dimensions of the computational mesh across the computational domain which encompasses the source region and the city of Athens (Attica region $45km \times 39km \times 30km$, Athens city $1.2km \times 1.4km \times 0.6km$ and Acropolis hill area $580m \times 380m \times 40m$, cf. also Figure 3); and (ii) the need of propagating relatively high frequencies through the computational domain in order to study the dominant features of the site response of the Acropolis and the Parthenon. The simulations have been carried out based on employing the open-source library SPEED which can handle sharp changes of the mesh size and locally varying polynomial approximation orders [12] allowing for an accurate and flexible description of the spatial variation of mechanical parameters and characteristic physical dimensions. [21].

A first set of simulations was carried out to ensure that the large-scale regional model assembled for this study could yield results consistent with the previous findings reported in [39], who investigated the seismic response of the Acropolis using a local model and high-frequency ($f_{max} = 30Hz$) plane-wave excitation. Encouraged by the good outcome of this preliminary check, we proceeded with two advanced numerical simulations of the 1999 Athens earthquake:

(a) ground shaking across the metropolitan area including the Acropolis hill;
(b) soil-structure interaction of the Acropolis and of the Parthenon.

3.1 Numerical model of the seismic source, regional crustal properties and geological setting

We adopted the kinematic representation of the seismic fault proposed in [33], where broadband seismograms recorded at regional distances are used to estimate the source features of the Athens 1999 M_w 5.9 mainshock, occurred on 7 September 1999. The earthquake had a normal faulting style, and most likely occurred on the Fili fault [40], one of the major tectonic features in the area [41]. In our study the total fault length and width are considered to be about $25km$. The average slip across the rupture area is $0.16m$, while the maximum slip approaches $1m$ in the proximity of the hypocenter (Figure 1). The rise time is equal to $0.3s$, while the rupture velocity is $2.7km/s$. Strike, dip and rake of the fault plane are 115°, 57°, −80° respectively. Consistent with [33], we use the hypocenter location of [32], at $8km$ depth. The geophysical properties of the 1D layered regional crustal model are the same used by [42] and [31]. The shear-wave velocity increases with depth, from $1.5km/s$ at the free surface to $3.6km/s$ at the bottom of the numerical model. The free surface of the model follows the regional geomorphology, smoothed starting from Shuttle Radar Topography Mission (SRTM) 1 Arc-Second ($30m$) global data. Water bodies are not included. Since a detailed representation of the complexity of the geological and seismotectonic settings of the regions of Attika and Athens is beyond the scope of this study, the model comprises only the dominant regional geological features, besides those crucial to the development of the case study at hand. In the Athens metropolitan area the model includes simplified representations of the Athenian Schist formation - a slightly metamorphosed series of Cretaceous marls and shales with lenses of sandstone and limestone - and of the recent deposits of the Athens basin, along with a high-resolution model of the limestone outcrop of the Acropolis. The geometry of the contact between recent deposits and bedrock was obtained from [43]. The extent of the Athenian Schist formation was derived merging information from [43, 44] and the 1:50,000 geological map of Greece (Athinai, Piraieus sheet). Our representation of the Athens Schist formation is necessarily gross and only aims at representing the overall footprint of the formation and its likely depth in the metropolitan area. The Acropolis hill is a block of late Cretaceous limestone resting on the Athenian Schist. The Acropolis ridge is well approximated by an ellipse elongated in the EW direction with major axis length $\sim 250m$ and minor axis length $\sim 150m$. The hill is characterized by very steep topography on the northern, eastern and southern edges, where the geomorphology is dominated by a $30-35m$ thick limestone outcrop and the average slope of the hill flanks exceeds 30°. Large portions of the Acropolis are covered by anthropic infill overlaying the limestone unit. The anthropic infill unit was not included in the model because the dominant frequencies ($> 10Hz$, see [45]) of its dynamic response are beyond the maximum frequency for which the computational grid was designed. The Parthenon and its foundation are made of porous-stone blocks with dry masonry structure, cf. [38]. The geophysical properties of the geomaterials as included in the numerical model are given in Table 2. Each ID block number of the computational model refers to a geophysical layer in which we assign the material and numerical parameters, see also Figure 3. In particular, given

z_q, $q = 0, 1, 2, 3$, that represent the projection of a generic point with coordinate z into the topografical surface, outcrop of the Acropolis, the Athenian basin and Schist, respectively, the properties of the first layer are described in Table 1 and Figure 2, where the different velocity profiles are in $[m/s]$ and the soil density in $[kg/m^3]$.

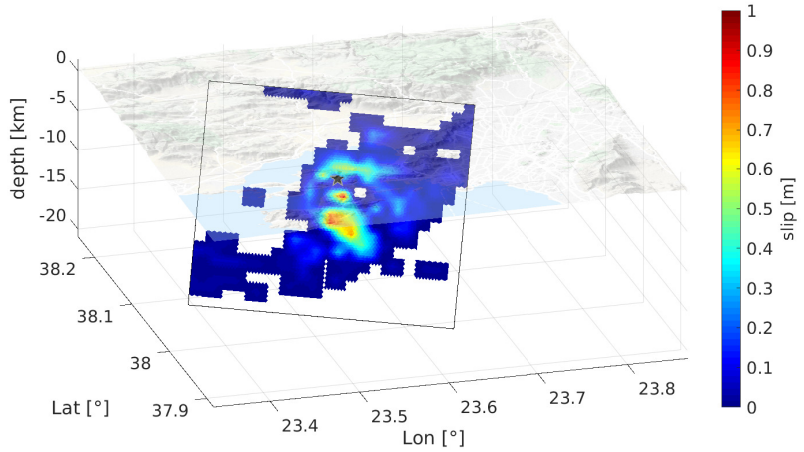

Fig. 1: Distribution of the slip amplitude values on the fault plane adapted from [33] and location of the hypocenter (star) adapted from [32].

Table 1: Properties of the first layer.

Sublayer	v_s $[m/s]$	v_p $[m/s]$	ρ $[kg/m^3]$
$z_1 < z \leq z_0,\ z \leq z_3$	1500	2670	2500
$z_2 < z \leq z_0$	380	760	1800
$z_3 < z \leq z_0,\ z \leq z_1,\ z \leq z_2$	700	1250	2300

3.2 Computational models setup

In order to be able to propagate accurately waves with a frequency content up to $f_{max} = 5Hz$, cf. [12, 21], we built a non-conforming mesh with size of $5 - 20m$ on the Acropolis hill, and of $70m$ in the metropolitan area of Athens. Outside the city and in the source region, the mesh size ranges from $200 - 300m$ within the topmost layer to $700m$ at depth, see Figure 3. The model consists of 1.319.941 hexahedral elements and, by using a polynomial approximation degree N_k varying

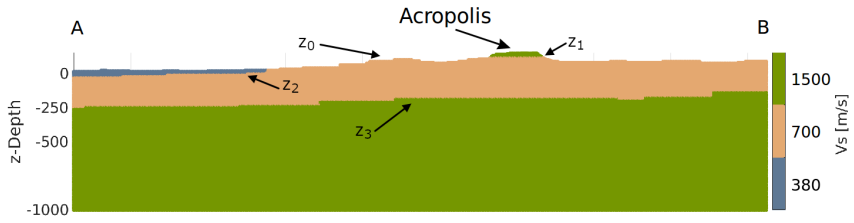

Fig. 2: Vertical cross-section along the East-West (EW) direction (see horizontal red line $A - B$ in Figure 3). z_q, $q = 0, 1, 2, 3$ represent the surfaces that delimit the sublayers with different material properties. z_1 outcrops of the Acropolis, z_2 and z_3 denote the Athenian basin and Schist, respectively.

from 1 to 4 (Tables 2 and 3), it has 253.599.612 degrees of freedom. We fixed the total observation time $T = 30s$ and we used a time step $\Delta t = 10^{-4}s$. The wall-time for the simulation was around 50 hours on 1024 cores on the Marconi cluster at CINECA, Italy (`https://www.hpc.cineca.it/hardware/marconi`).

In the second simulation we considered the previous computational model with the following simplification: homogeneous geophysical properties for the topmost layer ($v_s = 1500m/s$, $v_p = 2670m/s$ and $\rho = 2500kg/m^3$) with constant mesh size of $300m$. Then we integrated a simplified model of the Parthenon using a non-conforming mesh with size of $0.5m$ (Figure 4 and Table 4). The numerical model of this simulation has 738.109 hexahedral elements and, by choosing a first order polynomial degree for the computational mesh of the Parthenon $N_k = 1$, it has 127.900.548 degrees of freedom. The time step was $\Delta t = 10^{-5}s$. In this case the wall-time for the simulation was around 210 hours on 512 cores on the Galileo (`https://www.hpc.cineca.it/hardware/galileo`) and Marconi–100 cluster at CINECA, Italy (`https://www.hpc.cineca.it/hardware/marconi100`).

Table 2: Horizontally stratified crustal model.

Layer	ID	Depth $[km]$	v_s $[m/s]$	v_p $[m/s]$	ρ $[kg/m^3]$	ξ [mHz]	h_k $[m]$	N_k
1	1–3	top – 1	see Table 1	see Table 1	see Table 1	$50\pi/v_s$	see Table 3	see Table 3
2	4	1 – 2	2500	4450	2500	62.83	200–300	4
3	5	2 – 5	3200	5700	2840	49.09	700	4
4	6	5 – 18	3370	6000	2900	46.61	700	4
5	7	18 – 30	3600	6400	2980	43.63	700	4

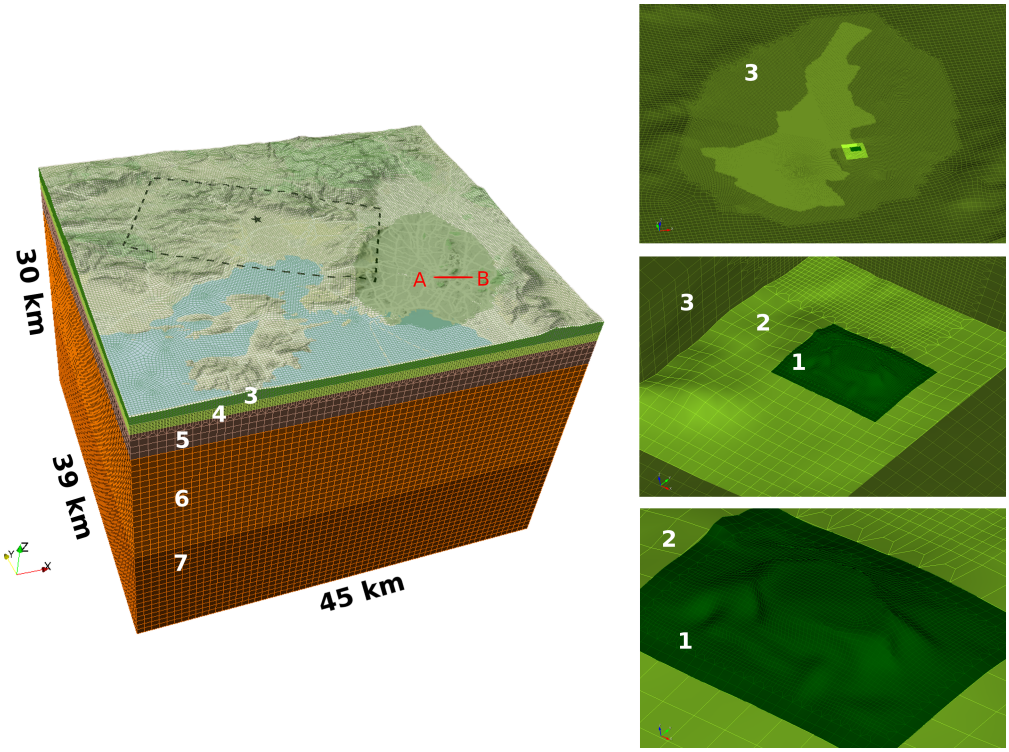

Fig. 3: 3D computational model for the Attika region with indication of the surface projection of the Fili fault and of the epicentre of the 1999 Athens earthquake, (left) and zoom on the Athens metropolitan area and Acropolis hill (right). Numbers denote ID blocks, see Tables 2 and 3.

Table 3: Horizontally stratified crustal model: zoom on first layer.

ID Block	h_k $[m]$	N_k
1	5 – 20	1
2	65	2
3	70 – 300	4

Table 4: Mesh size (h_k) and elastic properties of the Parthenon modelled as a single geophysical unit.

h_k $[m]$	N_k	v_s $[m/s]$	v_p $[m/s]$	ρ $[kg/m^3]$	ξ [mHz]
0.5	1	600	1000	2450	261.80

4 Numerical results and comparison with observed records

In the following, we discuss the results of our numerical simulations with emphasis on the characterization of earthquake ground motion and the seismic response of the Acropolis hill and the Parthenon.

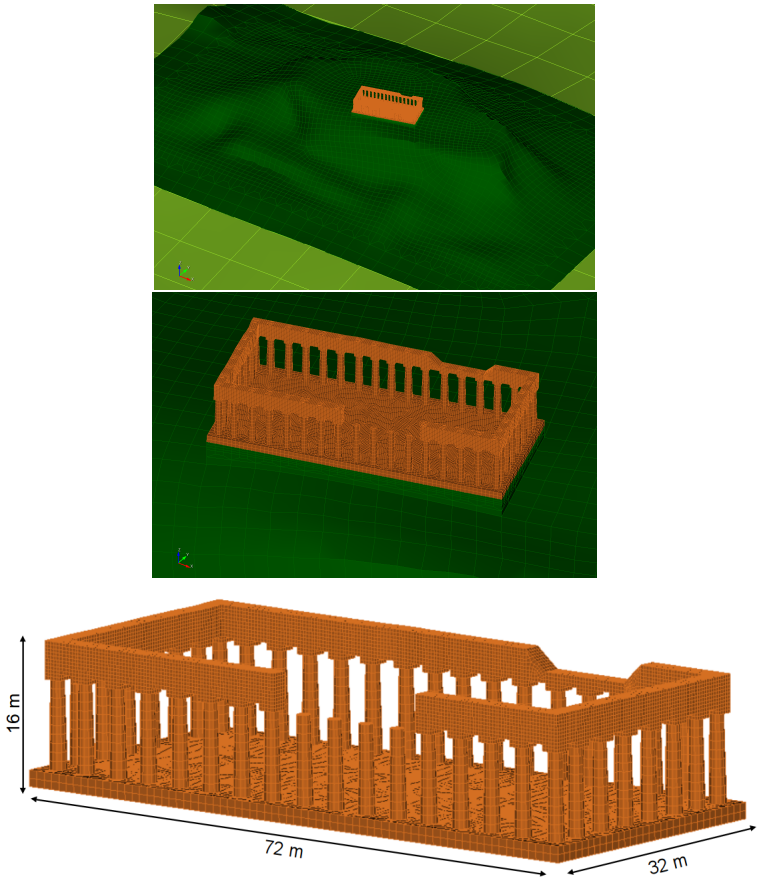

Fig. 4: 3D computational meshes of the Acropolis hill and the Parthenon.

4.1 Simulation of the 1999 Athens earthquake

Figure 5 depicts the spatial distribution of peak ground velocity (PGV, geometric mean of the two orthogonal horizontal components) generated by simulation (a), along with the surface projection of the seismogenic fault (dashed polygon) and the epicentre (star). The largest PGV values approach $46 cm/s$ closed to the source area and decrease to a few cm/s across the metropolitan area. On the Acropolis hill, the simulated PGV values are $6.5\, cm/s$. The figure shows the locations of seven strong-motion accelerographs operating at the time of the event. Information about these stations as retrieved from the Engineering Strong Motion Database [46] is given in Table 5, including the recorded PGV values.

We compare our results with those obtained through the global empirical ground motion model (GMM) CEA15 [45], as shown in Figure 6. The physics-based syn-

thetic (PBS) PGV values are color-coded according to the surface geology at the location of the synthetic receivers (the free surface nodes of the numerical mesh): green–limestone (L), orange–Athenian Schist (AS), blue–Athenian alluvial basin deposits (AB). We used $v_{s,30} = 1500m/s$ for the GMM, i.e., the v_s of the topmost layer of the crustal structure and of the Athens limestone. Consistent with the chosen GMM, the closest distance to the fault rupture (R_{rupt}) is used on the x-axis of Figure 6. The agreement with the GMM is remarkable, especially in the near-field region ($R_{rupt} \lesssim 20km$), where PBS and GMMs often tend to disagree. The comparison remains very good at larger distances: the rate of attenuation seems to be the same for the synthetics and the GMM; the median values of the PBS show a rather constant offset w.r.t. the GMM and are always within the standard deviation $\pm\sigma$ bounds of the GMM.

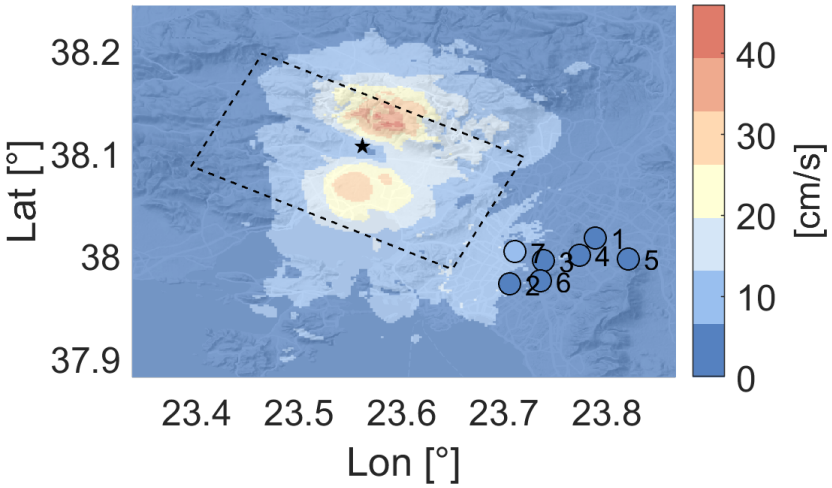

Fig. 5: Synthetic peak ground velocity PGV obtained as described in the text. Recorded PGV values for the stations in Table 5 have been superimposed.

The comparison of the synthetic waveforms generated by simulation (a) with the actual recordings of the 1999 Athens earthquake poses some challenges due to the simplified geological model used in the simulations and to the characteristics of the contemporary strong-motion monitoring infrastructure and associated data / metadata. The exact start time of the recordings is unknown, as are the actual orientation and polarity of the orthogonal horizontal components of the accelerographs. In spite of these difficulties, we propose in Figure 7 a comparison at station SGMA, located on the Athenian Schist formation in the iconic Syntagma Square. All data were filtered in the range $[0.5, 5]Hz$ using a causal Butterworth filter with order $N_f = 3$; the recorded data retrieved by the Engineering Strong-Motion Database were delayed by $1.1s$. The comparison is overall satisfactory, since the synthetics seismograms seem to capture well the orientation and polarity at the onset of ground shaking –

Table 5: List of stations in the area of Athens and comparison of PGV values from ShakeMap[a], and SPEED simulation The stations pertain to the seismic networks HI (ITSAK, 1981)[b] and HL (NOA-IG, 1975)[c].

ID	Code	Rec. PGV $[cm/s]$	Sim. PGV $[cm/s]$	Geology
1	ATH2	8.4	3.0	Athenian schist – limestone
2	ATH3	15.9	4.8	alluvium
3	ATH4	8.9	5.7	alluvium
4	ATHA	7.4	4.2	Athenian schist
5	DMKA	2.4	1.7	limestone
6	SGMA	13.6	4.9	Athenian schist
7	SPLB	21.5	8.1	alluvium

[a] https://earthquake.usgs.gov/earthquakes/eventpage/iscgem1655758/shakemap/pgv
[b] https://www.fdsn.org/networks/detail/HI/,
[c] https://www.fdsn.org/networks/detail/HL/

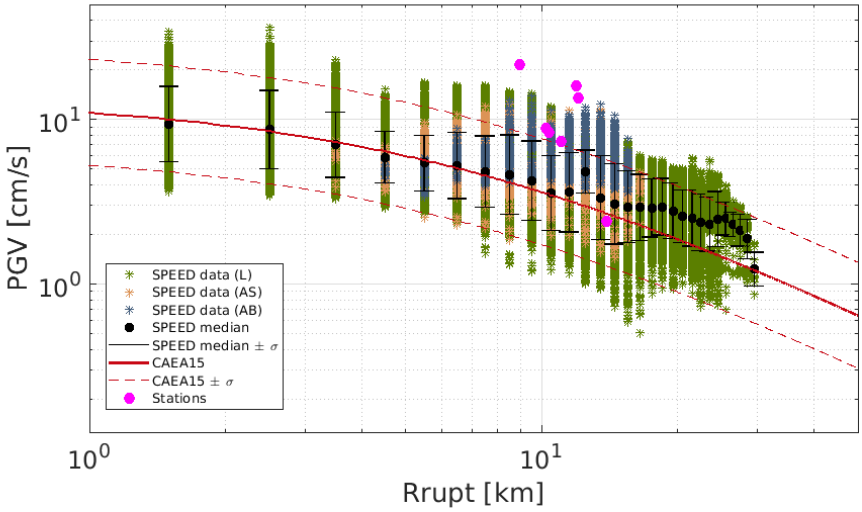

Fig. 6: Synthetic peak ground velocity PGV values compared with the empirical ground motion model of CEA15 [45] as explained in the text. Colored stars refer to PGV values at each receiver with assigned material properties: green–limestone (L), orange–Athenian Schist (AS), blue–Athenian alluvial basin deposits (AB). Recorded values for stations in Table 5 have been also superimposed.

the signature of the fault mechanism – and the dominant periods / frequencies of the recorded data both in the time and frequency domains. The recorded peak amplitudes are larger on the horizontal components, most likely due to amplification induced by small-scale geological features that are not included in the numerical models. The comparison of the Fourier Amplitude Spectra (FAS) of the vertical components hints a stronger vertical attenuation than in the numerical models.

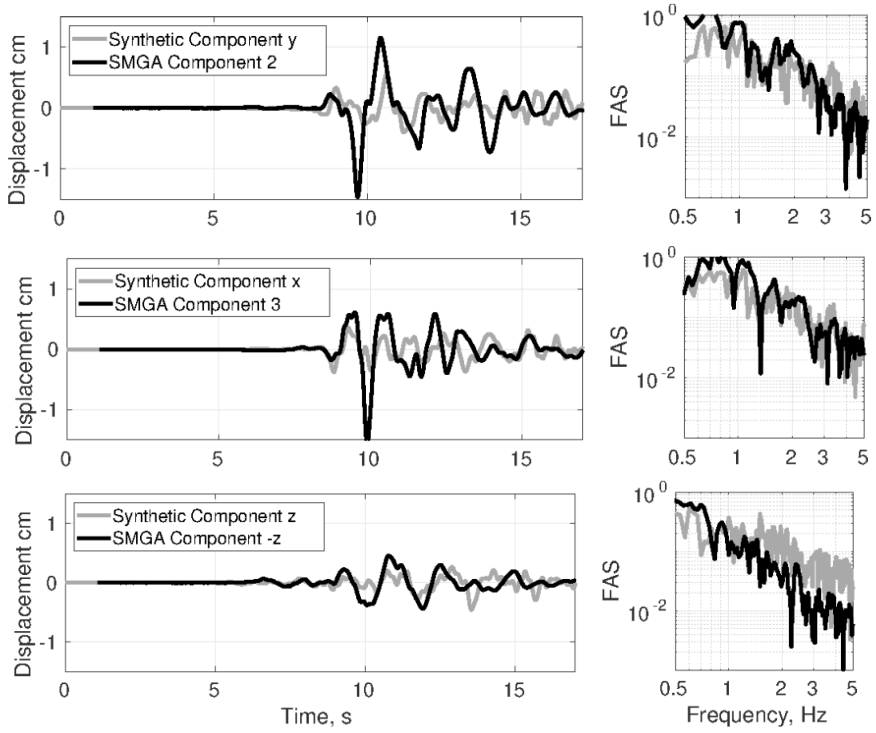

Fig. 7: Comparison of synthetic and recorded data at station SGMA (Syntagma Square ID 6) on Athenian Schist. Waveform data processed as described in the text. LHS panels: time-domain displacement waveforms; RHS panels: Fourier Amplitude Spectra (FAS).

4.2 Seismic response of the Parthenon

Simulation (b) was devoted to model at the same time the Athens 1999 earthquake and the shaking induced by the earthquake on the Parthenon. The Acropolis of Athens is monitored with a local network of strong-motion accelerographs operated by the Institute of Geodynamics, National Observatory of Athens (NOA-IG), in collaboration with the Acropolis Restoration Service (YSMA). The array consists of 10 strong-motion sensors (Guralp CMG-5TD) recording in continuous mode on 24-bit digitisers, sampling the main geological units constituting the Acropolis and including two sites devoted to monitoring monumental elements of the Parthenon (Table 6). In particular, stations C and B are located respectively at the crest and base of a marble column pertaining to the northern colonnade of the Parthenon. Even if the Acropolis array was not yet operational in 1999, the recordings of subsequent earthquakes and ambient vibration acquired since its installation allow

empirically assessing the key features of the seismic response of the Acropolis and the Parthenon, as, e.g., in [39]. Figure 8 shows the spectral ratios between station C and B. The curve shows the ratio (geometric mean of the horizontal components) as computed in [39] obtained from numerical simulation (b). The dominant frequencies at $\sim 1.5 - 2Hz$ of the empirical seismic response of the northern colonnade are well captured by the simulation, in agreement with [39], although the amplitude of the empirical spectral ratio is lower. Given the simplifications adopted in this to model the Parthenon as a homogeneous continuous geophysical unit, this result is quite remarkable and encouraging towards future improvements. To conclude, we report in Figure 9 some snapshots of the computed displacement field for the Attica region, including a zoom of the Acropolis and of the Parthenon. The displacement of the latter has been exaggerated by a factor 300 for visualization purposes.

Table 6: List of stations on the Acropolis hill.

Station code	Lat (°)	Lon (°)	Elevation $[m]$	Location	Geology
ACRB	37.9716	23.7265	159.8	Parthenon basement	porous stone blocks on limestone
ACRC	37.9716	23.7265	173.6	Parthenon N colonnade	(-)

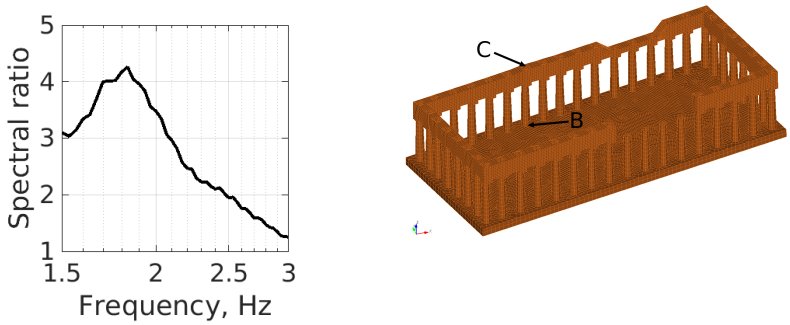

Fig. 8: Simulated spectral ratio at two stations (C, B), i.e. ACRC/ACRB, located respectively at the crest and base of a marble column pertaining to the northern colonnade of the Parthenon.

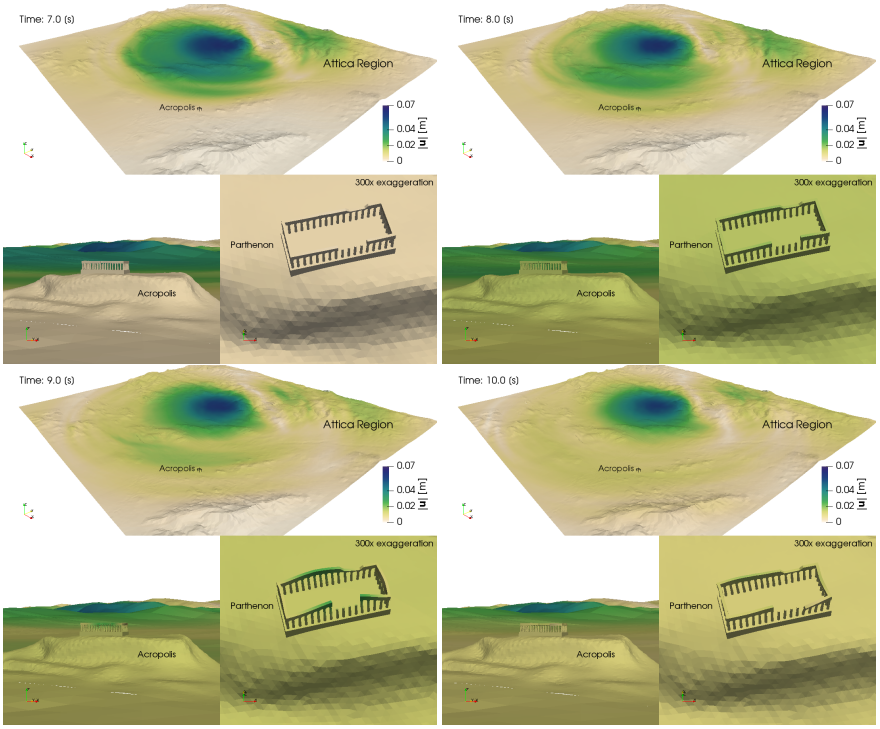

Fig. 9: Snapshots of the computed displacement field (absolute value) at four different time instants: $t = 7\ s$ (top-left), $t = 8\ s$ (top-right), $t = 9\ s$ (bottom-left) and $t = 10\ s$ (bottom-right). Displacement of the Parthenon has been exaggerated by a factor 300 for visualization purposes.

5 Conclusions and future developments

In this work we presented a first attempt of studying the seismic response of the Acropolis and of the Parthenon in Athens under the 1999 M_w 5.9 earthquake through the application of a DGSE method previously implemented in the open source library SPEED. SPEED offers major advantages for modeling multi-scale seismic scenarios, by relaxing constraints imposed by standard conforming spectral element methods and, therefore, reducing the simulation costs while attaining high order accuracy. To accomplish the multi-physics feature of the problem under investigation, we described the Athens 1999 earthquake with a set of simulations that try to capture the main features of the event and associated wave propagation. In order to obtain a realistic simulation of the physical phenomenon as a whole, the numerical model must be able to (i) provide a fault-rupture generation able to excite a broadband frequency spectrum; (ii) accurately propagate waves with a relatively high frequency content; (iii) to characterize the most important geological formations of the soil,

i.e. soft soil deposits and the Acropolis hill; (iv) accurately describe the geometry of major human built structures, such as the Parthenon. Having a computational model that accounts for all these details leads to enormous advantages from the modeling point of view, poses several challenges. First, although the grid generation process is facilitated by the possibility of using non-conforming meshes, it still requires significant effort to make sure that all the different spatial scales are correctly reproduced in the model. Second, the accurate representation of the high frequency wavefronts (from source to site) requires the use of very large computational domains (which can reach billions of unknowns). Third, the computational cost, i.e., time to solution, must be kept under control. In this sense, an implicit or locally explicit time integration scheme may improve the performance of the overall numerical discretization. Finally, as a further step to improve the model and to describe in a more realistic way the seismic response of the structures as well as the soil-structure interaction, refined geological models and non-linear rheological models will have to be taken into account. In this sense, the work presented is the first step in the direction of using three-dimensional multi-scale methods for the study of soil-structure interaction, from the seismic source to the site. Overall, in spite of the above limitations, numerical simulations can be considered as a tool for seismic risk mitigation strategies for cultural heritage.

Acknowledgements P.F. Antonietti has been partially funded by PRIN grants n. 201744KLJL and n. 20204LN5N5 funded by the Ministry for Universities and Research (MUR). P.F. Antonietti and I. Mazzieri also acknowledge the financial support given by INdAM-GNCS. L. Melas has been partially supported by IDEA League Student grant.
We acknowledge the CINECA HPC supporting under the ISCRA initiative for the availability of high performance computing resources and support. The authors would like also to thank Zafeiria Roumelioti for her valuable help in providing seismic slip data. The geological maps of Attica were kindly provided by Ioannis Kalogeras. The contribution of L. Melas was mainly carried out during her PhD position at the Department of Mathematics, Politecnico di Milano, Italy.

References

1. J. Douglas and H. Aochi. A survey of techniques for predicting earthquake ground motions for engineering purposes. *Surv. Geophys.*, 29(3):187, 2008.
2. E. Chaljub, E. Maufroy, P. Moczo, J. Kristek, F. Hollender, P.-Y. Bard, E. Priolo, P. Klin, F. de Martin, Z. Zhang, W. Zhang, and X. Chen. 3-D numerical simulations of earthquake ground motion in sedimentary basins: testing accuracy through stringent models. *Geophys. J. Int.*, 201(1):90–111, 2015.
3. P. Moczo, J. Kristek, M. Galis, E. Chaljub, and V. Etienne. 3-D finite-difference, finite-element, discontinuous-Galerkin and spectral-element schemes analysed for their accuracy with respect to P-wave to S-wave speed ratio. *Geophys. J. Int.*, 187(3):1645–1667, 2011.
4. N. A. Petersson and B. Sjögreen. High Order Accurate Finite Difference Modeling of Seismo-Acoustic Wave Propagation in a Moving Atmosphere and a Heterogeneous Earth Model Coupled Across a Realistic Topography. *J. Sci. Comput.*, 74(1):209–323, 2018.
5. P. Moczo, J. Kristek, and M. Gális. *The Finite-Difference Modelling of Earthquake Motions: Waves and Ruptures*. Cambridge University Press, 2014.

6. D. Komatitsch and J.-P. Vilotte. The spectral element method: an efficient tool to simulate the seismic response of 2D and 3D geological structures. *B. Seismol. Soc. Am.*, 88(2):368–392, 1998.
7. P. Galvez, J.-P. Ampuero, L. A. Dalguer, S. N. Somala, and T. Nissen-Meyer. Dynamic earthquake rupture modelled with an unstructured 3-D spectral element method applied to the 2011 M9 Tohoku earthquake. *Geophys. J. Int.*, 198(2):1222–1240, 2014.
8. M. Dumbser, M. Käser, and E. F. Toro. An arbitrary high-order Discontinuous Galerkin method for elastic waves on unstructured meshes-V. Local time stepping and p-adaptivity. *Geophys. J. Int.*, 171(2):695–717, 2007.
9. A. Breuer, A. Heinecke, S. Rettenberger, M. Bader, A. Gabriel, and C. Pelties. Sustained petascale performance of seismic simulations with seissol on supermuc. In J. M. Kunkel, T. Ludwig, and H. W Meuer, editors, *Supercomputing*, pages 1–18. Springer International Publishing, 2014.
10. K. Duru, L. Rannabauer, A.-A. Gabriel, G. Kreiss, and M. Bader. A stable discontinuous galerkin method for the perfectly matched layer for elastodynamics in first order form. *Numer. Math.*, 146(4):729–782, 2020.
11. S. Wolf, A.-A. Gabriel, and M. Bader. Optimization and local time stepping of an ader-dg scheme for fully anisotropic wave propagation in complex geometries. In *International Conference on Computational Science*, pages 32–45. Springer, 2020.
12. P. F. Antonietti, I. Mazzieri, A. Quarteroni, and F. Rapetti. Non-conforming high order approximations of the elastodynamics equation. *Comput. Methods Appl. Mech. Engrg.*, 209/212:212–238, 2012.
13. P. F. Antonietti, A. Ferroni, I. Mazzieri, R. Paolucci, A. Quarteroni, C. Smerzini, and M. Stupazzini. Numerical modeling of seismic waves by discontinuous spectral element methods. *ESAIM: Proceedings and Surveys*, 61:1–37, 2018.
14. P. F. Antonietti and I. Mazzieri. High-order Discontinuous Galerkin methods for the elastodynamics equation on polygonal and polyhedral meshes. *Comput. Methods Appl. Mech. Engrg.*, 342:414–437, 2018.
15. R. Paolucci, I. Mazzieri, and C. Smerzini. Anatomy of strong ground motion: Near-source records and three-dimensional physics-based numerical simulations of the Mw 6.0 2012 May 29 Po plain earthquake, Italy. *Geophys. J. Int.*, 203(3):2001–2020, 2015.
16. L. Evangelista, S. del Gaudio, C. Smerzini, A. d'Onofrio, G. Festa, I. Iervolino, L. Landolfi, R. Paolucci, A. Santo, and F. Silvestri. Physics-based seismic input for engineering applications: a case study in the Aterno river valley, Central Italy. *B. Earthq. Eng.*, 15(7):2645–2671, 2017.
17. R. Paolucci, I. Mazzieri, G. Piunno, C. Smerzini, M. Vanini, and A. G. Özcebe. Earthquake ground motion modeling of induced seismicity in the Groningen gas field. *Earthquake Eng. Struct. Dynam.*, 50(1):135–154, 2021.
18. R. Paolucci, I. Mazzieri, C. Smerzini, and M. Stupazzini. Physics-based earthquake ground shaking scenarios in large urban areas. In *Perspectives on European earthquake engineering and seismology*, pages 331–359. Springer, 2014.
19. P.F. Antonietti, I. Mazzieri, L. Melas, R. Paolucci, A. Quarteroni, C. Smerzini, and M Stupazzini. Three-dimensional physics-based earthquake ground motion simulations for seismic risk assessment in densely populated urban areas. *Math. Eng.*, 3(2):1–31, 2021.
20. M. Infantino, I. Mazzieri, A. G. Özcebe, R. Paolucci, and M. Stupazzini. 3D physics-based numerical simulations of ground motion in Istanbul from earthquakes along the marmara segment of the North Anatolian Fault. *Bull. seism. Soc. Am.*, 110(5):2559–2576, 2020.
21. I. Mazzieri, M. Stupazzini, R. Guidotti, and C. Smerzini. SPEED: SPectral Elements in Elastodynamics with Discontinuous Galerkin: a non-conforming approach for 3D multi-scale problems. *Internat. J. Numer. Methods Engrg.*, 95(12):991–1010, 2013.
22. R. Stacey. Improved transparent boundary formulations for the elastic-wave equation. *B. Seismol. Soc. Am.*, 78(6):2089–2097, 1988.
23. E. Faccioli, F. Maggio, R. Paolucci, and A. Quarteroni. 2D and 3D elastic wave propagation by a pseudo-spectral domain decomposition method. *J. Seismol.*, 1(3):237–251, 1997.

24. P. F. Antonietti, A. Ferroni, I. Mazzieri, R. Paolucci, A. Quarteroni, C. Smerzini, and M. Stupazzini. Numerical modeling of seismic waves by discontinuous spectral element methods. *ESAIM: Proceedings and Surveys*, 61:1–37, 2018.
25. D. N. Arnold, F. Brezzi, B. Cockburn, and L. D. Marini. Unified analysis of discontinuous Galerkin methods for elliptic problems. *SIAM J. Numer. Anal.*, 39(5):1749–1779, 2001/02.
26. B. Rivière and M. F. Wheeler. Discontinuous finite element methods for acoustic and elastic wave problems. In *Current trends in scientific computing (Xi'an, 2002)*, volume 329 of *Contemp. Math.*, pages 271–282. Amer. Math. Soc., Providence, RI, 2003.
27. B. Rivière, S. Shaw, and J. R. Whiteman. Discontinuous Galerkin finite element methods for dynamic linear solid viscoelasticity problems. *Numer. Methods Partial Differ. Equ.*, 23(5):1149–1166, 2007.
28. P. F. Antonietti, B. Ayuso de Dios, I. Mazzieri, and A. Quarteroni. Stability analysis of discontinuous Galerkin approximations to the elastodynamics problem. *J. Sci. Comput.*, 68(1):143–170, 2016.
29. P. F. Antonietti, A. Ferroni, I. Mazzieri, and A. Quarteroni. hp-version discontinuous Galerkin approximations of the elastodynamics equation. In *Spectral and high order methods for partial differential equations—ICOSAHOM 2016*, volume 119 of *Lect. Notes Comput. Sci. Eng.*, pages 3–19. Springer, Cham, 2017.
30. E. Lekkas. The Athens earthquake (7 september 1999): intensity distribution and controlling factors. *Eng. Geol.*, 59(3):297–311, 2001.
31. G.-A. Tselentis and J. Zahradnik. the Athens earthquake of 7 September 1999. *B. Seismol. Soc. Am.*, 90(5):1143–1160, 2000.
32. P. Papadimitriou, N. Voulgaris, I. Kassaras, G. Kaviris, N. Delibasis, and K. Makropoulos. The September 7, 1999 Athens earthquake sequence recorded by the Cornet Network: Preliminary results of source parameters determination of the mainshock. *Ann. Geol. Pays Hellen*, XXXVII:29–39, 2000.
33. Z. Roumelioti, D. Dreger, A. Kiratzi, and N. Theodoulidis. Slip distribution of the 7 September 1999 Athens earthquake inferred from an empirical Green's function study. *B. Seismol. Soc. Am.*, 93(2):775–782, 2003.
34. A. Anastasiadis, M. Demosthenous, C. Karakostas, N. Klimis, B. Lekidis, B.N. Margaris, C. Papaioannou, C. Papazachos, and N.P. Theodulidis. *The Athens (Greece) earthquake of September 7, 1999: preliminary report on strong motion data and structural response*. Multidisciplinary Center for Earthquake Engineering Research, 1999.
35. G.A. Papadopoulos, G. Drakatos, D. Papanastassiou, I. Kalogeras, and G. Stavrakakis. Preliminary results about the catastrophic earthquake of 7 September 1999 in Athens, Greece. *Seismol. Res. Lett.*, 71(3):318–329, 2000.
36. G. Gazetas. The 1999 Parnitha (Athens) Earthquake: soil effects on distribution of damage. *Lessons Learned from Recent Strong Earthquakes*, pages 5–18, 2001.
37. I. S. Kalogeras, C. P. Evangelidis, N. S. Melis, and K. Boukouras. The Athens Acropolis strong motion array. In *EGU General Assembly Conference Abstracts*, page 9523.
38. I. S. Kalogeras and D. Egglezos. Strong motion record processing for the Athenian Acropolis seismic response assessment. *Geotechnical Engineering for the Preservation of Monuments and Historic Sites*, pages 483–492, 2013.
39. C. Cauzzi, I. Kalogeras, N. Melis, M. Stupazzini, I. Mazzieri, and J. Clinton. Preliminary results on the seismic response of the Acropolis of Athens (Greece) through recorded earthquake data and numerical simulations. In *Proceedings of the 6th ICEGE*. Paper 637, 2015.
40. S.B. Pavlides, G. Papadopoulos, and A. Ganas. The fault that caused the Athens September 1999 Ms= 5.9 earthquake: Field observations. *Nat. Hazards*, 27(1-2):61–84, 2002.
41. A. Ganas, S.B. Pavlides, S. Sboras, S. Valkaniotis, S. Papaioannou, G.A. Alexandris, A. Plessa, and G.A. Papadopoulos. Active fault geometry and kinematics in Parnitha Mountain, Attica, Greece. *J. Struct. Geol.*, 26(11):2103 – 2118, 2004.
42. F. Gallovič and J. Brokešová. The k^2 rupture model parametric study: Example of the 1999 Athens earthquake. *Studia Geophys. et Geod.*, 48:589–613, 2004.
43. G. Koukis and N. Sabatakakis. Engineering geological environment of Athens, Greece. *Bull. Eng. Geol. Environ.*, 59(2):127–135, 2000.

44. A. Argyraki, E. Kelepertzis, G. Fligos, E. Athanasiou, K. Gardiakos, and V. Kourgia. Geochemical mapping of urban soils in Athens, Greece - Preliminary results. *BGSG*, 47(2):901–909, 2013.
45. C. Cauzzi, E. Faccioli, M. Vanini, and A. Bianchini. Updated predictive equations for broadband (0.01–10 s) horizontal response spectra and peak ground motions, based on a global dataset of digital acceleration records. *B. Earthq. Eng.*, 13(6):1587–1612, 2015.
46. G. Lanzano, L. Luzi, C. Cauzzi, J. Bienkowski, D. Bindi, J. Clinton, M. Cocco, M. D'Amico, J. Douglas, L. Faenza, C. Felicetta, F. Gallovič, D. Giardini, O.-J. Ktenidou, V. Lauciani, M. Manakou, A. Marmureanu, E. Maufroy, A. Michelini, H. Özener, R. Puglia, R. Rupakhety, E. Russo, M. Shahvar, K. Sleeman, and N. Theodoulidis. Accessing european strong-motion data : an update on ORFEUS coordinated services. *Seis. Res. Lett.*, 92(3):1642–1658, 2021.

MOX Technical Reports, last issues

Dipartimento di Matematica
Politecnico di Milano, Via Bonardi 9 - 20133 Milano (Italy)

50/2022 Elías, A.; Jiménez, R.; Paganoni, A.M.; Sangalli, L.M.
Integrated Depths for Partially Observed Functional Data

51/2022 Losapio, D.; Scotti, A.
Local Embedded Discrete Fracture Model (LEDFM)

52/2022 Fedele, M.; Piersanti, R.; Regazzoni, F.; Salvador, M.; Africa, P. C.; Bucelli, M.; Zingaro, A.; I
A comprehensive and biophysically detailed computational model of the whole human heart electromechanics

47/2022 Botti, M.; Di Pietro, D.A.; Salah, M.
A serendipity fully discrete div-div complex on polygonal meshes

49/2022 Botti, M.; Fumagalli, A.; Scotti, A.
Uncertainty quantification for mineral precipitation and dissolution in fractured porous media

48/2022 Gregorio, C.; Barbati, G.; Ieva, F.
A wavelet-mixed landmark survival model for the effect of short-term oscillations in longitudinal biomarker's profiles

45/2022 Franco, N.; Fresca, S.; Manzoni, A.; Zunino, P.
Approximation bounds for convolutional neural networks in operator learning

46/2022 Lucca, A.; Fraccarollo, L.; Fossan, F.E.; Braten, A.T.; Pozzi, S.; Vergara, C.; Muller, L.O.
Impact of pressure guidewire on model-based FFR prediction

44/2022 Peli, R.; Dovera, L.; Fighera, G.; Menafoglio, A.; Secchi, P.
Forecasting Oil Production Rates in Primary Depletion using the Physics-based Residual Kriging functional approach

43/2022 Zappon E.; Manzoni A.; Gervasio P.; Quarteroni A.
A reduced order model for domain decompositions with non-conforming interfaces